

# Mechanics of lithium metal at the nanoscale

Jack Aspinall<sup>1,2</sup>, David Armstrong<sup>1,2\*</sup>, and Mauro Pasta<sup>1,2\*</sup>

<sup>1</sup>Department of Materials, University of Oxford, Parks Road, Oxford OX1 3PH, United Kingdom

<sup>2</sup>The Faraday Institution, Quad One, Didcot, OX11 0RA, United Kingdom

\*Corresponding authors: david.armstrong@materials.ox.ac.uk  
mauro.pasta@materials.ox.ac.uk

## Abstract

The fracture of ceramic solid electrolytes, driven by the plating of lithium within cracks, has been identified as one of the fundamental issues to successfully develop solid-state batteries. Understanding the mechanics of lithium at the nanoscale is therefore essential. In this work, the elastic and plastic properties of lithium are measured by nanoindentation within an electron microscope. Lithium metal samples are characterised by electron backscattered diffraction (EBSD) before and after indentation to understand the dependence of the mechanical properties on crystallographic orientation, and determine the stiffness tensor components, moduli and Poisson's ratio using a method first proposed by Vlassak and Nix. The measured stiffness tensor components are  $C_{11}=13.3$ ,  $C_{12}=11.2$ , and  $C_{44}=8.8$  GPa. Hardness measurements show a clear size effect with hardness in excess of 100 MPa observed for indent depths below 300 nm, which could contribute toward observed lithium filament propagation.

## Introduction

The fracture of solid electrolytes by lithium metal filaments penetration is a well-documented failure mode of lithium metal batteries [1–3]. Yet it seems counterintuitive for filaments of lithium metal, one of the softest metals [4], to be able to fracture stiff ceramics. The fracture process in lithium metal batteries is inherently a nanoscale effect. By directly probing the mechanical properties of lithium using nanoindentation, we can better understand the mechanical interaction occurring between lithium metal and the solid electrolyte.

The mechanical response of lithium consists of a recoverable/elastic component and a permanent/plastic component. Lithium's elastic response is fully described by its stiffness tensor  $C$ , which has 3 independent components  $C_{11}$ ,  $C_{12}$  and  $C_{44}$ . The tensor allows the resultant elastic strain to be calculated from any given stress tensor. Elasticity is independent of length-scale. Four works have measured the three independent elastic constants of lithium ( $C_{11}$ ,  $C_{12}$  and  $C_{44}$ ); which

together fully describe the material's anisotropic elastic response [5–8]. Overall, these works suggest tensor components in the range  $C_{11}=12.3\text{--}14.5$  GPa,  $C_{12}=10.2\text{--}11.3$ , and  $C_{44}=8.5\text{--}8.9$  GPa. This suggests lithium is a highly elastically anisotropic material ( $A \approx 8$ ). Most mechanical works on lithium metal have studied polycrystals, with Young's modulus values ranging from 4.97 GPa [9] to 9.8 GPa [10]. Notably several studies have measured values close to 7.8 GPa [11–13]. Given lithium's high elastic anisotropy, it is surprising that there is such strong agreement between measurements of polycrystalline Young's modulus in studies with different sample preparation and testing methodologies. Taking the average of prior single crystal studies ( $C_{11}=13.4$ ,  $C_{12}=11.0$ ,  $C_{44}=8.7$  GPa) gives a Hill estimate of 10.8 GPa, which is typically a good estimate for untextured polycrystalline moduli [14]. 7.8 GPa lies 28% below this expected value. The disparity between single crystal and polycrystal elastic properties as well as the range of single-crystal values reported in the literature justifies new work quantifying the stiffness tensor.

Lithium's plastic response is complex, depending on the mobility of micron-scale dislocations. At small length scales relevant for lithium filaments, the number of dislocations within the stressed volume is limited and therefore size-dependent hardness is expected. Several works have studied plasticity in lithium in micron-scale to bulk samples, and at a range of strain rates. This is summarised well in the recent paper by Fincher et al. [15]. Collectively, studies find bulk lithium has a yield stress of 0.6 MPa, increasing by around a factor of two with high strain rate [12, 13, 15–17].

With decreasing plastic zone size, the hardness of lithium increases by over an order of magnitude. Xu et al. performed nanopillar compression to investigate size-dependent hardness, measuring an increase in yield stress from 15 to 105 MPa [8] as pillar size decreases from 9.45  $\mu\text{m}$  to 1.39  $\mu\text{m}$ . The pillars were prepared by focused ion beam milling (FIB) which raises concerns that ion-implantation from pillar machining [18] is contributing to an increase in hardness, especially for the small pillars. In typical materials such as molybdenum, the effect of ion-beam damage on measured mechanical properties is negligible [19], but due to lithium's low atomic mass, the penetration depth of FIB ions is significantly higher. Our stopping range of ions in matter (SRIM [20]) calculations suggest a mean ion implantation depth of  $102 \pm 20$  nm in Li compared to  $11 \pm 6$  nm in Mo with a 30 kV  $\text{Ga}^+$  beam. The phase diagram of lithium and gallium is complex with many intermetallics that may form [21]. The contribution of this FIB-damaged shell to the observed hardness is unclear. Nevertheless, the trend agrees with micro indentation work [10, 15] and similar experiments on other metals [22]. In the sub-micron region relevant for lithium filament initiation there is a broad spread of results, with yield stress varying from 8 MPa [10] to over 100 MPa [8] between different studies. More work is needed at this length scale to quantify size-dependent plasticity in lithium metal.

A summary table of room temperature lithium metal mechanical properties studies is available in the supporting information (Table S1).

In this work, using a nanoindenter within a scanning electron microscope (SEM), we have correlated nanoindentation with electron backscattered diffraction (EBSD) mapping of lithium metal to allow the orientation dependence of the mechanical response to be measured at the nanoscale. Using well established mathematics [23],

these measurements have allowed us to calculate the elastic stiffness tensor of lithium, getting values of  $C_{11}=13.3$ ,  $C_{12}=11.2$ ,  $C_{44}=8.8$  GPa. We simultaneously measure hardness and observe strong size dependence, with hardness in excess of 100 MPa observed for indent depths below 300 nm. We discuss the impact of these results on lithium filament propagation into stiff ceramic electrolytes.

## Results and discussion

Using very sharp microtome blades we were able to prepare fresh lithium surfaces, with a surface roughness of  $38 \pm 2$  nm (Table S2), which we were able to successfully EBSD (Figure 1A). The colouring of each pixel denotes the crystal lattice orientation relative to the sample normal at that point, calculated from the Kikuchi diffraction pattern (Figure 1B). The orientation is shown in the inverse pole figure (Figure 1C). This preparation method may be useful for other studies on lithium, such as in the preparation of samples for atomic force microscopy (AFM)[24]. In the map shown in Figure 1A, 78% of the 29400 points indexed successfully. It can be observed from the map that points near lateral grain boundaries, are rarely resolved. Electron cross section scales strongly with atomic number [25], so lithium having the lowest electron cross section of all metals, represents a limit case for EBSD. A detailed discussion of the implications for this on EBSD mapping is provided in the supporting information.

Having successfully EBSD mapped lithium metal samples, arrays of indents were performed within large grains. Figure 2A and B show an example indent array's continuous stiffness measure of modulus and the array's corresponding EBSD map. A schematic of the experiment is shown in Figure 2C. By averaging the modulus data for each set, we can obtain a point in surface orientation – modulus space, as shown on the inverse pole figure in Figure 2D. The averages of measured indentation modulus for multiple indentations within grains of differing orientation, plotted in Figure 2D, show the expected trend of mechanical indentation anisotropy for cubic crystals, with indents along vectors near the  $\langle 100 \rangle$  axis of the crystal having lower moduli (11 GPa) than those near the  $\langle 111 \rangle$  direction (14 GPa). A Nelder-Mead minimisation algorithm was used to obtain a least-squares fit, giving fitted values of the stiffness tensor of  $C_{11}=13.3$ ,  $C_{12}=11.2$  and  $C_{44}=8.8$

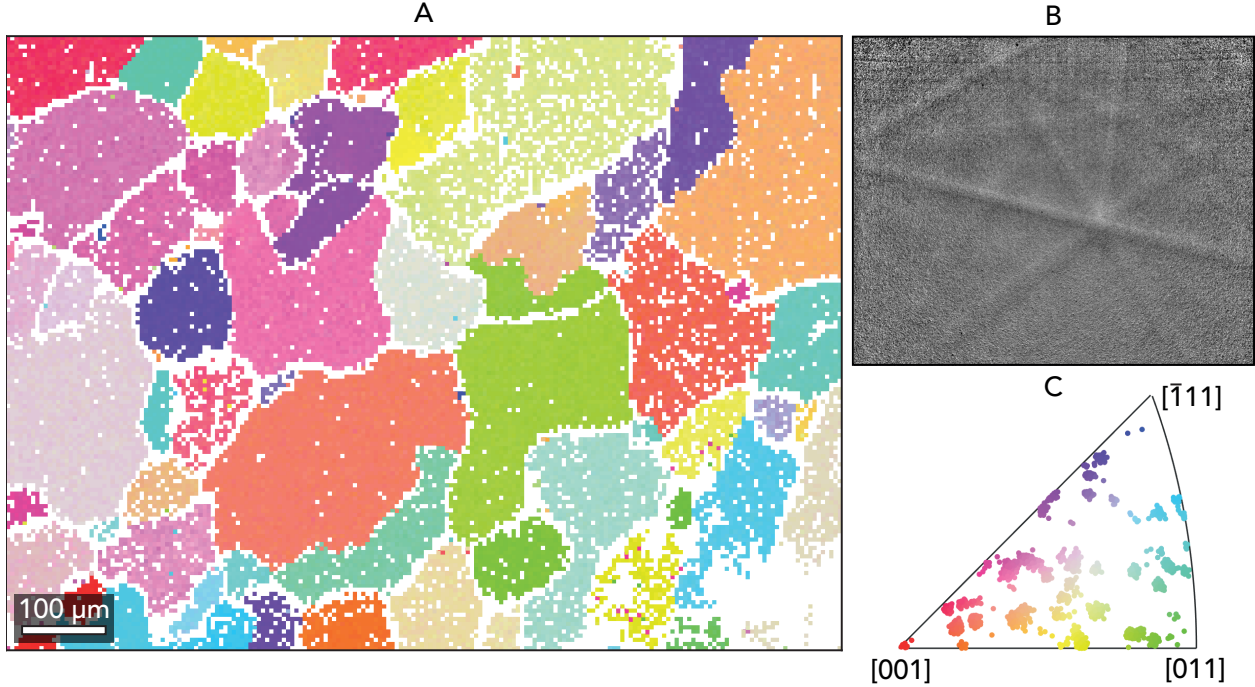


**Figure 1.** EBSD of lithium metal. A - EBSD map showing large, equiaxed grains of lithium metal. B - Example Kikuchi pattern imaged by EBSD detector. C - Inverse pole figure for shown map showing orientation of crystal lattice for points in the map.

GPa (see Experimental Procedures for details).

To visualise the resultant fit, the indentation modulus curve for grains with surface normals lying in the  $\{110\}$  plane has been calculated, with its maximum along the  $\langle 111 \rangle$  vector at 54 degrees as shown in Figure 2E. The eight experimental grain orientations with surface normal lying near the  $\{110\}$  planes (top and right edges of D) have also been plotted. The error bars represent the standard deviation of the indentation modulus values for the indents within each grain's indent set. The three stiffness matrix components fully describe the elastic response of the material, and other values such as polycrystalline Young's, shear and bulk moduli can be calculated from them. In the table, the two extreme single crystal uniaxial Young's moduli values in the  $[100]$  and  $[111]$  directions have been calculated with approximately a factor of seven difference.

Our elastic stiffness tensor results sit in the middle of the range of measured/calculated indentation results [6–8], and are in very good agreement with the work by the group of Slotwinski and Felice [6, 7]. The work shows lithium is highly elastically anisotropic. Implementing the full stiffness tensor

(measured in this work), allows the elastic response of the material to be precisely determined across length scales for any general stress state, with numerical tools such as Abaqus. The knowledge of lithium's elastic anisotropy also allows worst-case mechanical scenarios to be modelled, e.g. single-crystal lithium filaments compressed in the  $[111]$  direction will act differently to those compressed in the  $[100]$  direction.

Practically, lithium's high elastic anisotropy and large grain size means that the stiffness of the material is strongly dependent on the texture. The Reuss and Voigt estimates for polycrystalline Young's moduli of lithium using our measured values are 6.41 GPa and 14.81 GPa. We would therefore reasonably expect a true polycrystal to have a Young's modulus of 10.6 GPa (arithmetic mean). The significant difference between the two estimates shows that the arrangement of grains of different orientations can have a substantial effect on the sample's modulus – this is confirmed by the wide range of literature values for stiffness of polycrystalline lithium summarised in the supporting information table (Table S1). Due to its softness, lithium is typically prepared by rolling which induces strong  $[100]$  out-of-plane texture into

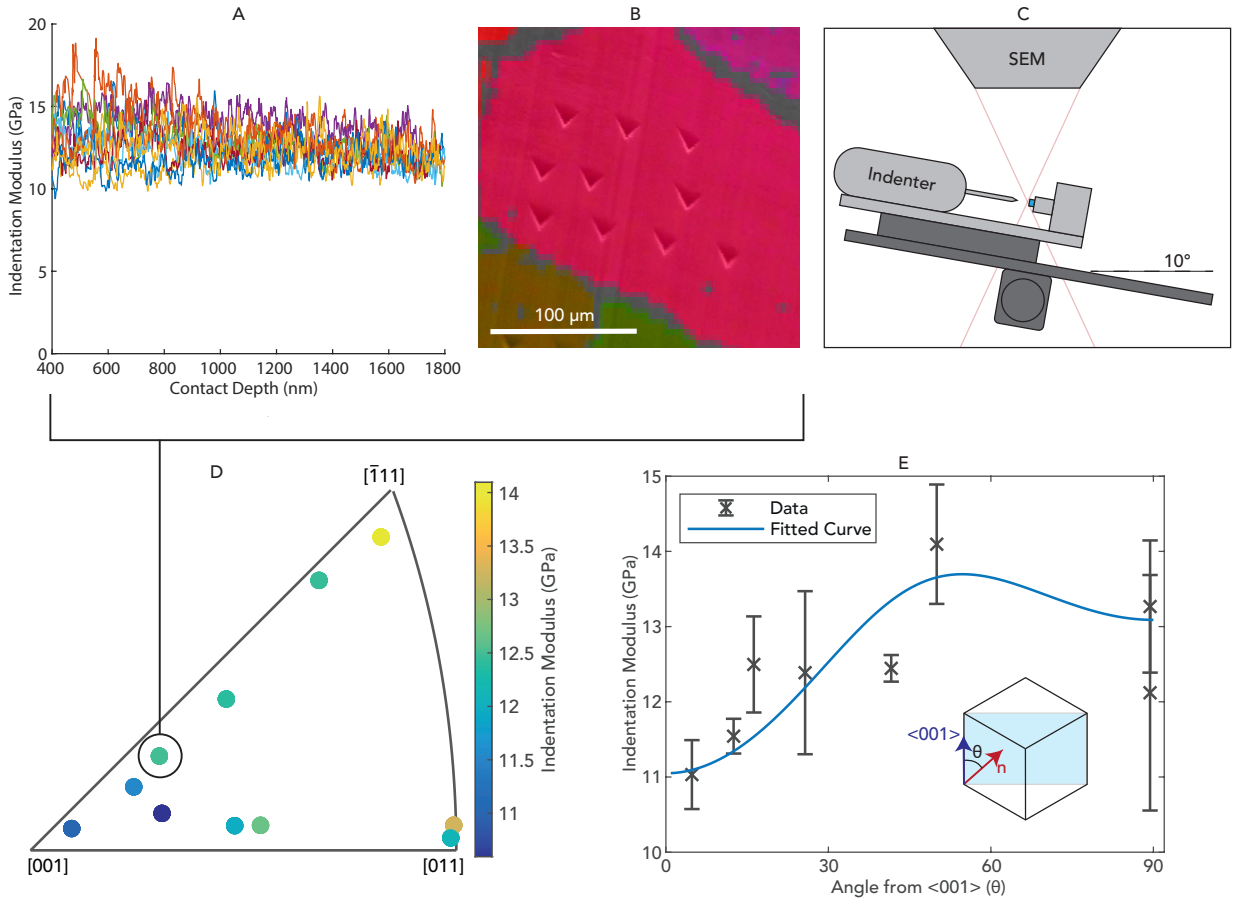


**Figure 2.** Orientation dependent elastic moduli of lithium metal. A – Measured indentation modulus vs depth for one grain. B – Corresponding EBSD map superimposed on SEM image of indented grains. C – Schematic showing experimental setup during indentation. D – Indentation modulus inverse pole figure showing orientation dependence of measured indentation modulus. E – Measured moduli for the eight indented grains with surface normal near  $\{110\}$  planes plotted against angle from  $<001>$  vectors, predicted trendlines from previous stiffness data and this works best-fit result plotted. Schematic inset in E to show theta definition.

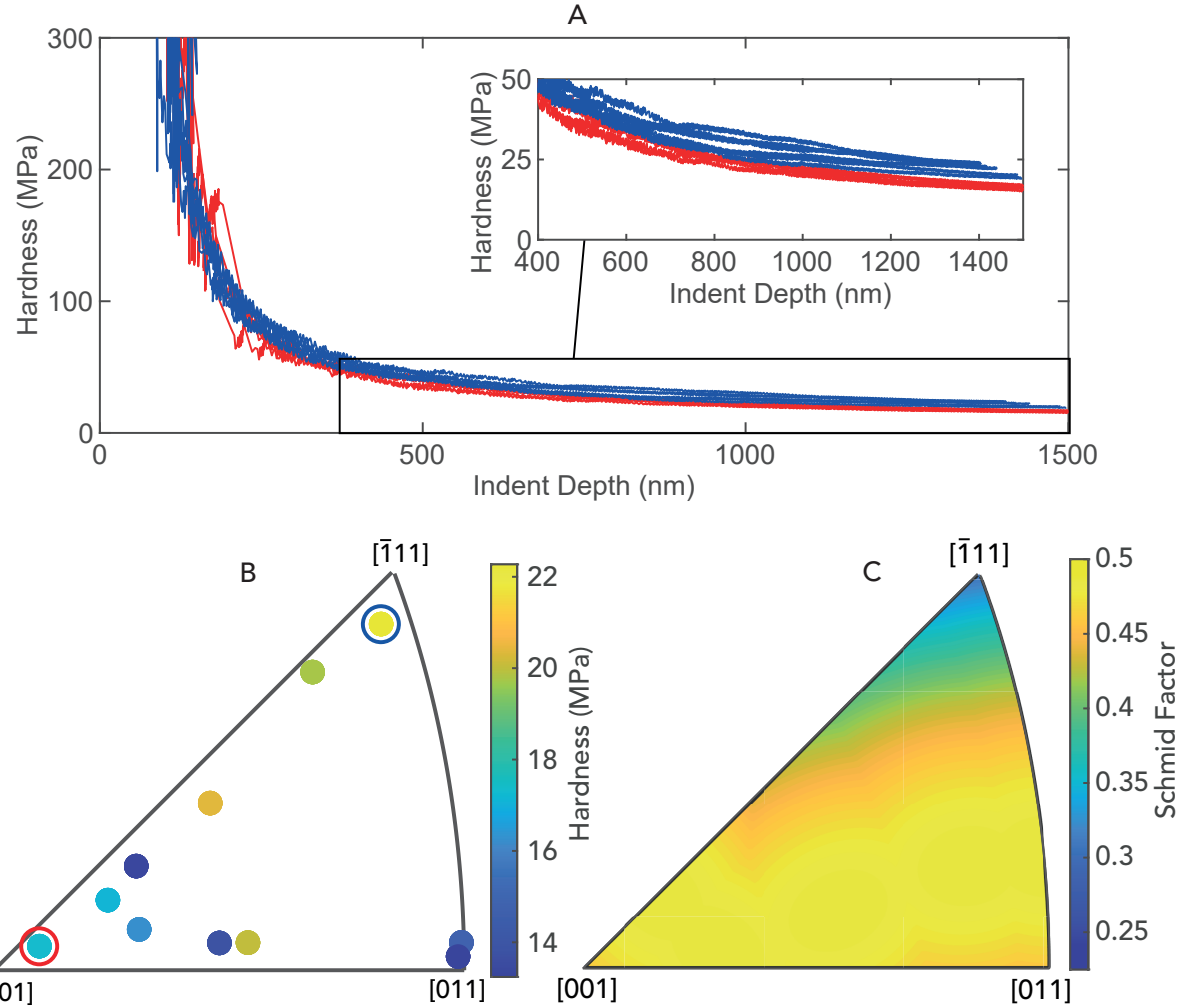
Property	$C_{11}$	$C_{12}$	$C_{44}$	$E[100]$	$E[111]$	A	$\nu$	B	E	G
Value	13.34	11.19	8.83	3.1	21.2	8.21	0.28/0.41	11.9	6.41/14.81	2.27/5.73

Table 1: Elastic properties results for pure lithium metal tested by nanoindentation.  $\nu$ , B, E and G are values for untextured lithium polycrystalline sample properties, with the two values being the Reuss and Voigt estimates respectively. All values are given in GPa, except A and  $\nu$  which are dimensionless.

the material [26], a direction in which its stiffness is much lower. The different polycrystalline moduli values obtained in the literature can be explained by the expected texture in the samples based on the processing method such as wire drawing or foil rolling

[17], the large grain size of lithium ( $\approx 100 \mu\text{m}$  [27]) and the error in the measurements.

The continuous measurement technique gives hardness (load/contact area) with depth, throughout the indentation. This provides a good approximation



**Figure 3.** Size and orientation dependent hardness of lithium metal measured by nanoindentation. A – Measured hardness vs indentation depth for indents in grains near [100] and [111]; as highlighted in B. B – Inverse pole figure showing orientation dependence of measured hardness averaged between 1.2 and 1.5 micrometers. C – Inverse pole figure showing Schmid factor of lithium metal assuming equal activation energy on {110}, {123} and {112} slip planes.

for the stresses evolved during rapid lithium plating within a crack. As can be seen in Figure 3A, there is a strong depth dependence on the measured hardness due to the size of indentation being of the same magnitude as a dislocation. Such depth dependence is well described by the equation first put forward by Nix and Gao in 1998 (Equation (1) [28]), tending to a hardness of  $H_0$  at high depth, with a characteristic decay length  $h^*$ . When fitting the data beyond 500 nm, where the indentation error is small, the hardness curves for all indents follow this expression. At low

depths (<500 nm), where deviation from this trend is often observed [29], measured hardness values slightly exceed the curve. The average values for all indents, and the standard deviations, are  $H_0=2.01\pm0.16$  MPa and  $h^*=97.8\pm42.1$   $\mu\text{m}$ .

$$H = H_0 \sqrt{1 + \frac{h^*}{h}} \quad (1)$$

As can be seen in Figure 3A, hardness curves from different grain orientations are very similar, but a slight hardness anisotropy between lattice

orientations is observed, with the average hardness between 1.2 and 1.5 micron for each indentation direction varying from 22.3 MPa in the  $<111>$  indentation axis to 17.2 MPa near  $<100>$ , as plotted in Figure 3A, with the corresponding points on the inverse pole figure circled (Figure 3B). The measured anisotropy of hardness corresponds well with the calculated Schmid factor of the axis of indentation, for the  $\{110\} <111>$ ,  $\{112\} <111>$  and  $\{123\} <111>$  slip systems of the body-centred cubic (BCC) crystal structure – as shown in the Figure 3C. Where the Schmid factor is low, the hardness is high. This is intuitive, given the critically resolved shear stress on the slip plane is proportional to the Schmid factor and the applied stress; and therefore, for a lower Schmid factor, a larger normal force is needed to drive slip [30].

We observed adhesion between the indentation tip and the sample, such that a negative load was needed to detach the tip from the sample. The mean value of this pull-off force was  $-532.6 \pm 0.8 \mu\text{N}$  and mean pull off stress was  $7.95 \pm 0.02 \text{ MPa}$ . No clear trend with orientation was observed. Published work on Berkovich indentation adhesion is limited to ideal elastic systems such as polydimethylsiloxane (PDMS) [31] so the mathematics is not applicable for plastic materials such as lithium. Approximating the indenter as a rigid flat punch ( $r = \sqrt{A_c/\pi}$ ), and using the Kendall model ( $P_{\text{off}} = \sqrt{8A_cMW_{\text{ad}}R}$ ) [32], the work of adhesion is  $9.61 \pm 0.03 \text{ mJ/m}^2$ . This should only be taken as an estimate. We are not aware of any other quantitative reports of adhesion with lithium.

Size dependent plasticity is a well-established component of dislocation theory, the effect is widely observed in metallic nanoindentation studies [28] and has recently been highlighted in mechanical studies on lithium at length scales between 1 and  $10 \mu\text{m}$  [8, 10, 15]. The data we have presented in this paper demonstrates that on the  $\approx 200 \text{ nm}$  length scale relevant for lithium filaments, the hardness is approximately 100 MPa. The flow stress of nanoscale lithium can be approximated as a third of the measured hardness [33], approximately 30 MPa.

Previous experimental work has demonstrated crack propagation by lithium deposition within the crack under a compressive stress – evidenced by subsequent viscoplastic extrusion of lithium out of the crack [3], a good example is reproduced in Figure 4B. If lithium is under a compressive pressure, an equal opening pressure must be exerted on the solid electrolyte, this is shown schematically in

Figure 4A. As ceramic solid electrolytes are stiff, the crack opening forces are redistributed leading to a stress concentration at the crack tip. Considering the simple filled crack case, linear elastic fracture mechanics equations for an edge crack experiencing internal pressure can be used [34, 35] ( $K_1 = \Psi\sigma\sqrt{\pi a}$ , where  $K_1$  is the stress concentration at the crack tip,  $\sigma$  crack opening pressure,  $a$  crack length and  $\Psi$  a geometry factor of approximately one). Solid electrolytes are typically stiff ceramics, with low fracture toughness values ( $K_{1c}$ ) in the range  $0.5\text{-}1 \text{ MPa}\sqrt{\text{m}}$  [36–39], with the notable exception of LiPON - which seems to have a high fracture toughness [38]. Assuming a maximum flaw size of  $5 \mu\text{m}$ , a uniform crack opening pressure of 30 MPa is too small to cause catastrophic fracture in solid electrolyte materials ( $K_1 < 0.12 \text{ MPa}\sqrt{\text{m}}, K_{1c}$ ). By this analysis, this suggests lithium plating should not be able to fracture the current crop of ceramic electrolytes.

There are three possible explanations for the observed fracture in ceramic solid electrolytes on lithium plating.

First, it may be for very high currents and very small crack diameters ( $<100 \text{ nm}$ ), the higher stresses evolved at higher strain rates than we have tested here, are sufficient to drive fracture. A crack opening stress of 200 MPa and a crack length of  $5 \mu\text{m}$  will fracture materials with a fracture toughness below  $0.8 \text{ MPa}\sqrt{\text{m}}$ .

Second, to yield lithium out of a crack, forces at the lithium-ceramic interface will need to be overcome in addition to overcoming the material's intrinsic yield stress (von-Mises yield criterion). The magnitude of the adhesion measured here suggests these forces may be significant. The situation is analogous to forging where the average pressure needed grows exponentially with the friction coefficient and aspect ratio.

Third, most experimental works demonstrating lithium filament propagation and concurrent electrolyte fracture, show a progressive degradation over successive cycles, instead of catastrophic fracture on the first [1, 3, 40, 41]. This matches the well-established concept of crack growth under a sub-critical but cyclic load, where the crack growth per cycle in the main (stage II) regime is described by the Paris-Erdogan law. As such, cyclic stresses caused by lithium plating and stripping from within a crack on successive cycles, will propagate the crack across the electrolyte. Below a threshold stress

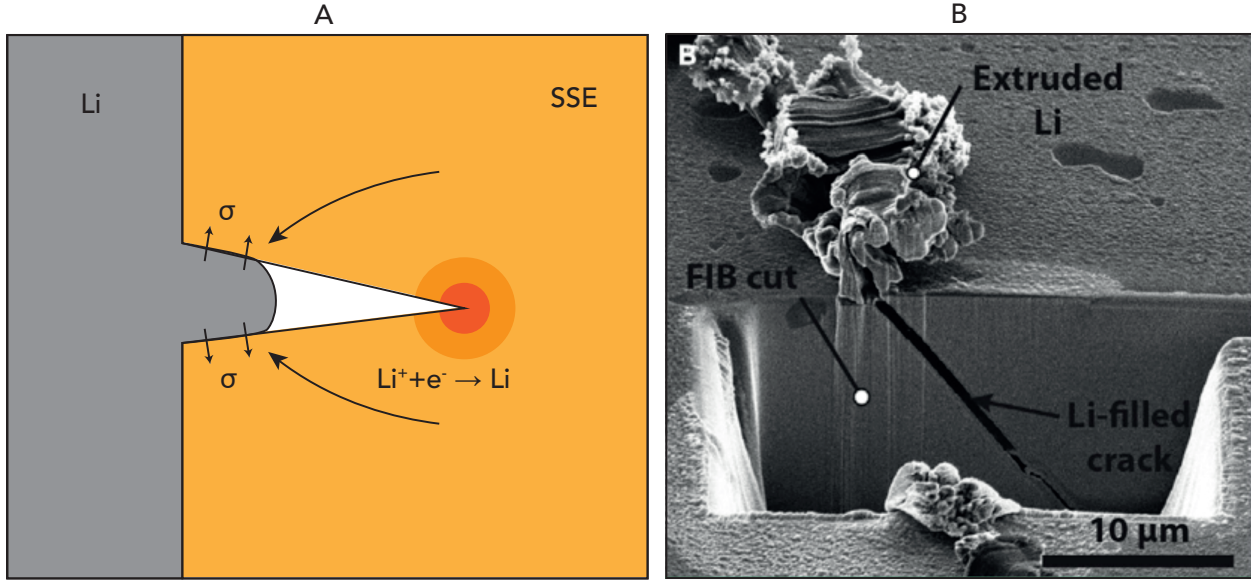


**Figure 4.** Relevance of nanoscale hardness to solid electrolyte fracture, due to lithium plating within cracks. A - Schematic of stress concentration due to redistributed crack opening stress from lithium plated within a crack in a solid-state electrolyte SSE. B – Image reproduced from Kazyak et al. [3] showing lithium-filled crack of width <500 nm in high-density  $\text{Li}_7\text{La}_3\text{Zr}_2\text{O}_{12}$  (LLZO), and subsequent Li extrusion.

concentration amplitude, crack growth is negligible in ceramics – this threshold value is a materials property which should be investigated for candidate solid electrolyte materials. There are no current studies of this type on solid electrolyte materials.

Further work is needed to model the mechanical interaction between lithium metal and solid-state electrolytes, and we hope the results in this work can inform these more accurate models. In the meantime, higher fracture toughness electrolytes should be pursued. The hardness results in this work suggest that electrolytes which can tolerate cyclic loads of the order of 100 MPa, for as many cycles as the battery is intended to perform, should be pursued.

## Concluding remarks

In this work we have quantified the mechanics of lithium at the nanoscale by nanoindentation. Our measurements suggest stiffness tensor components of  $C_{11}=13.3$ ,  $C_{12}=11.2$ ,  $C_{44}=8.8$  GPa. Clear size dependent hardness is observed due to the stressed volume being small enough so that few dislocations experience a shear stress and therefore less slip occurs than would for a bulk test. A hardness greater

than 100 MPa is observed on the length-scale of lithium filaments, this is two orders of magnitude higher than the bulk measured yield stress of 0.6 MPa [15]. Linear elastic fracture mechanics suggest crack opening stresses of this order are likely to fracture current solid electrolyte materials due to their relatively low fracture toughness, especially over successive cycles.

## Experimental procedures

### Lithium sample preparation

All work was performed within MBraun gloveboxes (<0.1 ppm O<sub>2</sub> and H<sub>2</sub>O). To prepare the lithium samples, 0.5g of lithium metal foil (Alfa Aesar, 99.9% foil) was melted at 250 degrees Celsius within a custom-made stainless-steel crucible, lined with stainless steel foil and with a stainless-steel lid, in a furnace (MTI OTF-1200X-S-II) within a glovebox, before removing from the furnace to air cool. The stainless-steel liner was peeled away to extract the solidified ingot. Test samples of approximate size 5 mm x 5 mm x 2 mm were cut from the centre of the ingots using a scalpel and mounted to 5 mm aluminium SEM stubs using a small amount of

two-part epoxy (Araldite). Surfaces were prepared using fresh polytetrafluoroethylene (PTFE) coated microtome blades (Epredia<sup>TM</sup> Shandon<sup>TM</sup>) with a table-top vice as a guide. The cut sample surface was aligned perpendicular to the indentation axis using the SEM optics to within 0.5 degrees in both tilt axes. AFM measurements gave a surface roughness of  $38 \pm 2$  nm for a 25-micron square scan size.

## Microscopy

Scanning electron microscopy (SEM) characterisation and nanoindentation were performed within a single contained system consisting of a Bruker Hysitron PI88 in-situ nanoindenter, with a five-axis sample stage mounted to the five-axis stage of a Tescan Mira-3 FEG-SEM with Oxford Instruments EBSD and EDS detectors. The SEM chamber opens into a dedicated MBraun argon glovebox, enabling sample change without air exposure. EBSD was performed at a beam voltage of 20 kV, current of 500 nA, tilt of 70 degrees and a working distance of 15 mm. The two five-axis stages of the indentation setup allow the sample to be rotated between EBSD and indentation positions. The system allows indents to be performed at distinct sites. Only large grains with good EBSD band contrast were tested, any indents accidentally placed on or near grain boundaries were excluded from analysis.

## Stopping range of ions in matter calculations

The implantation depth of gallium ions in both lithium and molybdenum were calculated using open-source SRIM-2013 software. The trajectories of 10,000 ions were calculated in each case, with a beam voltage of 30 kV.

## Indentation

Indentation was performed using a diamond Berkovich indentation tip (Hysitron), which was scanned with the AFM to extract a cross-sectional area function used in the calculation of reduced modulus and hardness from the measured stiffness, displacement, and load. The tip was cleaned before each test under a microscope. The nanoindenter was carefully calibrated to ensure quantitatively accurate results. Machine compliance was measured to be 8.02 nm/mN. Prior to each test, thermal drift rate was measured in contact, with preload of 10  $\mu$ N, over

40 seconds. The first 20 seconds was given as time for the system to stabilise after initial contact, and the last 20 seconds sampled to calculate mean drift rate, assumed constant throughout the test. A continuous modulus stiffness measurement frequency of 70 Hz was used, as it gave the lowest spread in phase shift and displacement amplitude, of frequencies from 30-300 Hz. A large dynamic load amplitude of 50  $\mu$ N at a target quasistatic load of 1000  $\mu$ N was used scaling with the square root of quasistatic load to minimise visco-plasticity error whilst retaining indenter contact [42, 43]). Because the continual stiffness measurement method captures both the load and unload segment of the oscillation, the effect of creep on measured stiffness is small. Indentation modulus values were obtained by averaging the stiffness measured between 1000 nm and 1500 nm of depth – with the indentation modulus calculated using an adapted version of the equation presented by Oliver and Pharr [44] for anisotropic materials (Equation (2)). Due to lithium's E/H value being so large, the choice of epsilon used to calculate the contact area ( $A_c$ ) makes negligible difference to the values of indentation modulus, so the standard 0.75 is used. The measured moduli of each of the indents within a grain were averaged to give a mean value of indentation modulus for each grain.

$$M = \frac{\sqrt{\pi}}{2} \frac{S}{\sqrt{A_c}} \quad (2)$$

To determine elastic stiffness tensor components, we have used the mathematics outlined in the 1994 Vlassak and Nix paper. The product of the load distribution under an indenter, and the displacement field of an elastic half-space boundary from a unit load applied on that boundary derived by Barrett and Lothe [45], is integrated over the contact region at the half-space boundary. The mathematics involves defining the sample surface normal ( $\hat{u}$ ) in the Cartesian system with its three axes along the principle  $<100>$  axes of the crystal, the surface normal vector is calculated from the Euler angles from EBSD as in Equation (3). This vector defines the boundary of an infinite half-space. Next, the integral in Equation (4) is computed where gamma is the angle between a vector  $t$ , which lies in the half-space boundary and starts at the origin, and some fixed datum in the half-space boundary. The matrix  $\beta$  is itself defined by Equation (5), with  $m$  and  $n$  being two perpendicular vectors to  $t$ , such that they form a right-handed cartesian set, with the

integral over phi summing the contributions for all orientations of  $\mathbf{m}$  and  $\mathbf{n}$  in the plane. The matrices of type  $(\mathbf{ab})$  are defined by the final Equation (6), with  $C$  being the elastic stiffness tensor. The indices are converted by the convention  $11 \rightarrow 1, 22 \rightarrow 2, 33 \rightarrow 3, 12 \rightarrow 4, 23 \rightarrow 5, 13 \rightarrow 6$ .  $\alpha$  is the cosine of the direct angle between the surface normal and the axis of the subscript. Einstein notation is used throughout, such that repeat indices in a single term denote a sum over 1 to 3. The original mathematics assumes a circular contact area to simplify the maths, and therefore a corrective factor of 1.06 is applied to account for the triangular shape of the Berkovich tip [23]. In the 30 years since its publication, this method has proved to be accurate across a range of materials [46, 47].

$$\hat{\mathbf{u}} = \begin{bmatrix} \sin(\psi)\sin(\Phi) \\ -\cos(\psi)\sin(\Phi) \\ \cos(\Phi) \end{bmatrix} \quad (3)$$

$$M = 1.06 \times 16\pi^2 \left( \int_0^{2\pi} \alpha_m \beta_{km}^{-1}(\gamma) \alpha_k d\gamma \right)^{-1} \quad (4)$$

$$\beta_{km}(\mathbf{t}) = \frac{1}{8\pi^2} \int_0^{2\pi} \{ (\mathbf{mm})_{js} - (\mathbf{mn})_{jk} (\mathbf{nn})_{kr}^{-1} (\mathbf{nm})_{rs} \} d\phi \quad (5)$$

$$(\mathbf{ab})_{jk} = a_i C_{ijkm} b_m \quad (6)$$

As such, the calculated indentation modulus solely depends on the orientation of the sample surface normal relative to the crystal lattice, and the stiffness matrix of the material. This numerical calculation was implemented in a Matlab script, allowing the generation of a predicted measured modulus surface in orientation space from given stiffness coefficient values. The set of values for  $C_{11}, C_{12}$  and  $C_{44}$  that gave the least squares fit to the orientation-modulus data were found using a Nelder-Mead algorithm, using a tetragonal simplex, implemented in the fminsearch function in MATLAB with a threshold value for all three of the stiffness components of 0.1.

## Data processing

EBSD data was processed using Oxford Instruments Aztec software, and the MTEX Matlab package, giving orientation data as a set of 3 Euler angles following the anticlockwise rotation ZX'Z" convention. Nanoindentation data was processed with Bruker's Triboscan software and Matlab, and

inverse pole figure graphs plotted with the MTEX Matlab package. Reuss and Voigt estimates were also calculated with MTEX.

## Acknowledgements

This work was supported by the Faraday Institution [grant numbers FIRG007, FIRG026, FIRG014 and FITG019-B]. Equipment including the indenter was funded by the Henry Royce Institute (through UK Engineering and Physical Science Research Council grant EP/R010145/1). We acknowledge Dr J E Darnbrough for initial work argon-ion polishing lithium for EBSD, and Prof. A J Wilkinson for first suggesting microtome.

## Author contributions

Conceptualisation, J.A., D.E.J.A and M.P.; Methodology, J.A; Investigation, J.A. Writing – Original Draft, J.A.; Writing – Review Editing, J.A., D.E.J.A and M.P.; Funding Acquisition, M.P.; Resources, D.E.J.A., M.P. Supervision, D.E.J.A and M.P.

## Declaration of interests

The authors declare no competing interests.

This work was supported by the Faraday Institution [grant numbers FIRG007, FIRG026, FIRG014 and FITG019-B]. Equipment including the indenter was funded by the Henry Royce Institute (through UK Engineering and Physical Science Research Council grant EP/R010145/1). The authors thank Dr J E Darnbrough for initial work argon-ion polishing lithium for EBSD, and Prof. A J Wilkinson for first suggesting microtome.

## Competing Interests

The authors declare no competing interests.

## References

1. Hao, S. *et al.* Tracking lithium penetration in solid electrolytes in 3D by in-situ synchrotron X-ray computed tomography. *Nano Energy* **82**, 105744 (2021).

2. Pasta, M. *et al.* 2020 roadmap on solid-state batteries. *JPhys Energy* **2**, 032008 (2020).
3. Kazyak, E. *et al.* Li Penetration in Ceramic Solid Electrolytes: Operando Microscopy Analysis of Morphology, Propagation, and Reversibility. *Matter* **2**, 1025–1048 (2020).
4. Schultz, R. *Lithium: Measurement of Young's Modulus* tech. rep. November (Fermi National Accelerator Laboratory, 2002).
5. C. Nash, H. & Smith, C. S. Single-crystal elastic constants of lithium. *Journal of Physics and Chemistry of Solids* **9**, 113–118 (1959).
6. Slotwinski, T. & Trivisonno, J. Temperature dependence of the elastic constants of single crystal lithium. *Journal of Physics and Chemistry of Solids* **30**, 1276–1278 (1969).
7. Felice, R. A., Trivisonno, J. & Schuele, D. E. Temperature and pressure dependence of the single-crystal elastic constants of Li and natural lithium. *Physical Review B* **16**, 5173–5184 (1977).
8. Xu, C., Ahmad, Z., Aryanfar, A., Viswanathan, V. & Greer, J. R. Enhanced strength and temperature dependence of mechanical properties of Li at small scales and its implications for Li metal anodes. *Proceedings of the National Academy of Sciences of the United States of America* **114**, 57–61 (2017).
9. Bridgman, P. W. The Electrical Resistance of Metals under Pressure. *Proceedings of the American Academy of Arts and Sciences* **57**, 41–66 (1922).
10. Herbert, E. G., Hackney, S. A. & Dudney, N. J. Nanoindentation of high-purity vapor deposited lithium films : The elastic modulus, 1335–1346 (2018).
11. Robertson, W. M. & Montgomery, D. J. Elastic modulus of isotopically-concentrated lithium. *Physical Review* **117**, 440–442 (1960).
12. Tariq, S., Ammigan, K., Hurh, P. & Schultz, R. *Li Material Testing - Fermilab Antiproton Source Lithium Collection Lens* in *Proceedings of the 2003 Particle Accelerator Conference* (2003), 1452–1454.
13. Masias, A., Felten, N., Garcia-Mendez, R., Wolfenstein, J. & Sakamoto, J. Elastic, plastic, and creep mechanical properties of lithium metal. *Journal of Materials Science* **54**, 2585–2600 (2019).
14. Kamaya, M. A procedure for estimating Young's modulus of textured polycrystalline materials. *International Journal of Solids and Structures* **46**, 2642–2649 (2009).
15. Fincher, C. D., Ojeda, D., Zhang, Y., Pharr, G. M. & Pharr, M. Mechanical properties of metallic lithium: from nano to bulk scales. *Acta Materialia* **186**, 215–222 (2020).
16. Hull, D. & Rosenberg, H. M. The deformation of lithium, sodium and potassium at low temperatures: Tensile and resistivity experiments. *Philosophical Magazine* **4**, 303–315 (1959).
17. LePage, W. S. *et al.* Lithium mechanics: Roles of strain rate and temperature and implications for lithium metal batteries. *Journal of the Electrochemical Society* **166**, 89–97 (2019).
18. Lee, J. Z. *et al.* Cryogenic Focused Ion Beam Characterization of Lithium Metal Anodes. *ACS Energy Letters* **4**, 489–493 (2019).
19. Shim, S., Bei, H., Miller, M. K., Pharr, G. M. & George, E. P. Effects of focused ion beam milling on the compressive behavior of directionally solidified micropillars and the nanoindentation response of an electropolished surface. *Acta Materialia* **57**, 503–510 (2009).
20. Ziegler, J. F., Ziegler, M. D. & Biersack, J. P. SRIM - The stopping and range of ions in matter (2010). *Nuclear Instruments and Methods in Physics Research, Section B: Beam Interactions with Materials and Atoms* **268**, 1818–1823 (2010).
21. Azza, H., Selhaoui, N., Iddaoudi, A. & Bouirden, L. Thermodynamic Reassessment of the Gallium–Lithium Phase Diagram. *Journal of Phase Equilibria and Diffusion* **38**, 788–795 (2017).
22. Rogne, B. R. & Thaulow, C. Strengthening mechanisms of iron micropillars. *Philosophical Magazine* **95**, 1814–1828 (2015).
23. Vlassak, J. J. & Nix, W. Measuring the Elastic Properties of Materials By Means of Indentation. *J. Mech. Phys. Solids* **42**, 1223–1245 (1994).
24. Kitta, M. & Sano, H. Real-Time Observation of Li Deposition on a Li Electrode with Operando Atomic Force Microscopy and Surface Mechanical Imaging. *Langmuir* **33**, 1861–1866 (2017).

25. Tabata, T., Andreo, P. & Shinoda, K. An analytic formula for the extrapolated range of electrons in condensed materials. *Nuclear Instruments and Methods in Physics Research, Section B: Beam Interactions with Materials and Atoms* **119**, 463–470 (1996).
26. Shi, F. *et al.* Strong texturing of lithium metal in batteries. *Proceedings of the National Academy of Sciences of the United States of America* **114**, 12138–12143 (2017).
27. Brodusch, N., Zaghib, K. & Gauvin, R. Electron backscatter diffraction applied to lithium sheets prepared by broad ion beam milling. *Microscopy Research and Technique* **78**, 30–39 (2015).
28. Nix, W. D. & Gao, H. Indentation size effects in crystalline materials: A law for strain gradient plasticity. *Journal of the Mechanics and Physics of Solids* **46**, 411–425 (1998).
29. Pharr, G. M., Herbert, E. G. & Gao, Y. The indentation size effect: A critical examination of experimental observations and mechanistic interpretations. *Annual Review of Materials Research* **40**, 271–292 (2010).
30. Ziegenhain, G., Urbassek, H. M. & Hartmaier, A. Influence of crystal anisotropy on elastic deformation and onset of plasticity in nanoindentation: A simulational study. *Journal of Applied Physics* **107** (2010).
31. Jin, Y., Zhu, B., Lu, Z., Liu, N. & Zhu, J. Challenges and recent progress in the development of Si anodes for lithium-ion battery. *Advanced Energy Materials* **7**, 1–17 (2017).
32. Jiang, Y., Grierson, D. S. & Turner, K. T. Flat punch adhesion: Transition from fracture-based to strength-limited pull-off. *Journal of Physics D: Applied Physics* **47** (2014).
33. Busby, J. T., Hash, M. C. & Was, G. S. The relationship between hardness and yield stress in irradiated austenitic and ferritic steels. *Journal of Nuclear Materials* **336**, 267–278 (2005).
34. Sneddon, I. N. & Elliot, H. A. The opening of a Griffith crack under internal pressure. *Quarterly of Applied Mathematics* **4**, 262–267 (1946).
35. Sakamoto, M. An Elastic Layer with a Penny-Shaped Crack Subjected to Internal Pressure. *JSME International Journal Series A* **46**, 10–14 (2003).
36. Wolfenstine, J., Allen, J. L., Sakamoto, J., Siegel, D. J. & Choe, H. Mechanical behavior of Li-ion-conducting crystalline oxide-based solid electrolytes: a brief review. *Ionics* **24**, 1271–1276 (2018).
37. Jackman, S. D. & Cutler, R. A. Effect of microcracking on ionic conductivity in LATP. *Journal of Power Sources* **218**, 65–72 (2012).
38. Kalnaus, S., Westover, A. S., Kornbluth, M., Herbert, E. & Dudney, N. J. Resistance to fracture in the glassy solid electrolyte Lipon. *Journal of Materials Research* **36**, 787–796 (2021).
39. Nonemacher, J. F., Naqash, S., Tietz, F. & Malzbender, J. Micromechanical assessment of Al/Y-substituted NASICON solid electrolytes. *Ceramics International* **45**, 21308–21314 (2019).
40. Ning, Z. *et al.* Visualizing plating-induced cracking in lithium-anode solid-electrolyte cells. *Nature Materials* **20**, 1121–1129 (2021).
41. Porz, L. *et al.* Mechanism of Lithium Metal Penetration through Inorganic Solid Electrolytes. *Advanced Energy Materials* **7** (2017).
42. Merle, B., Higgins, W. H. & Pharr, G. M. Critical issues in conducting constant strain rate nanoindentation tests at higher strain rates. *Journal of Materials Research* (2019).
43. Phani, P. S., Oliver, W. C. & Pharr, G. M. Understanding and modeling plasticity error during nanoindentation with continuous stiffness measurement. *Materials and Design* **194**, 108923 (2020).
44. Oliver, W. & Pharr, G. An improved technique for determining hardness and elastic modulus using load and displacement sensing indentation experiments. *Journal of Materials Research* **7**, 1564–1583 (1992).
45. Barnett, D. M. & Lothe, J. Dislocations and line charges in anisotropic piezoelectric insulators. *Physica Status Solidi (B)* **67**, 105–111 (1975).
46. Wang, W. & Lu, K. Nanoindentation study on elastic and plastic anisotropies of Cu single crystals. *Philosophical Magazine* **86**, 5309–5320 (2006).

47. Alkorta, J. & Sevillano, J. G. Assessment of elastic anisotropy and incipient plasticity in Fe 3C by nanoindentation. *Journal of Materials Research* **27**, 45–52 (2012).